Die Grenzen der Chemie neu ausloten? It takes #HumanChemistry

Wir suchen kreative Chemikerinnen und Chemiker, die mit uns gemeinsam neue Wege gehen wollen – mit Fachwissen, Unternehmertum und Kreativität für innovative Lösungen. Informieren Sie sich unter:

evonik.de/karriere

EVONIK
Leading Beyond Chemistry

A Novel Approach to Robustly Determine Residual Stress in Additively Manufactured Microstructures Using Synchrotron Radiation

Behzad Aminforoughi, Sebastian Degener, Julia Richter, Alexander Liehr,* and Thomas Niendorf

In recent decades additive manufacturing (AM) for years has been in focus of academia and industry as its underlying production principle allows for the realization of designs of unprecedented geometrical complexity. However, often such structures are not realized due to the lack of understanding of structural and mechanical properties, this fact amongst others related to the unique microstructures established by the related processes. In this context, residual stresses, highly affected by the scan strategy and process parameters used, play an essential role. Generally, various methods and approaches can be used to determine residual stress states experimentally. However, especially in case of the unique microstructures formed by AM, most standard procedures cannot be applied reliably. Commonly used methods based on X-ray diffraction rely on laboratory X-ray sources and synchrotron radiation. In present work, a novel method is proposed for robustly calculating residual stresses based on the linear regression method (similar to the $\sin^2\psi$ approach in reflection mode). Data obtained by use of synchrotron radiation in transmission mode are applied. To assess the reliability of the novel procedure, results are validated using simulations and in situ tensile tests. For these tests the well-known Ni-base alloy INCONEL 718 processed by laser powder bed fusion (LPBF), being characterized by a complex microstructure, and a conventionally manufactured 100Cr6 steel sample are used.

1. Introduction

1.1. Microstructure of Additively Manufactured Materials

Additive manufacturing (AM) is the subject of many recent publications.[1–3] Typical representatives of AM methods for the processing of metallic metals are mainly divided into three categories: wire feeding, powder feeding, and powder bed fusion systems.[3] The latter technique enables the production of metallic structures by layer-wise melting of a thin metal powder bed only using AM equipment and a sliced model generated by a computer-aided design (CAD) program. The application of a powder bed in powder-based AM technology facilitates the selective processing of individual layers in complex geometry. The most commonly used powder bed fusion techniques are selective electron beam powder bed fusion (EPBF) and laser powder bed fusion (LPBF).[3,4] EPBF structures are produced in a vacuum atmosphere and at a high temperature, eventually leading to a relatively low residual stress level. In contrast, LPBF processes usually take place at temperatures up to 200 °C. The localized energy input and the small melt pool sizes, respectively, in combination with low build chamber temperatures result in high temperature gradients, whereby residual stresses are favored.[5]

Generally, the influence of scan vectors and related strategies is a complex topic, which crucially has to be dealt with. Scan vector lengths, orientations, the order of rotation within a specific layer, and its subsequent layers are variables in every building process. Only a very limited number of comprehensive studies have reported on the effect of the scan strategy on the density, microstructure, mechanical properties, and residual stresses of LPBF parts, as clearly stated in previous studies.[5–8] Already an increased scan path length, e.g., due to a change of cross-section of a part, can result in a severely decreased relative density as well as fundamentally changed microstructure.[9,10]

The influence of parameters on the evolution of residual stresses was already numerously studied.[11,12] The authors showed that the residual stresses are mainly influenced by cooling rates, temperature gradients, and melt pool sizes. Also, a minimization of the temperature gradient by powder bed preheating is an option to reduce process-induced stresses.[1,13] The high influence of the laser power and the effect of scan strategies have been characterized.[14] The authors of that study

B. Aminforoughi, S. Degener, J. Richter, A. Liehr, T. Niendorf
Institute of Materials Engineering-Metallic Materials
University of Kassel
Kassel 34125, Germany
E-mail: liehr@uni-kassel.de

applied a stripe and a chess-board strategy on their samples. The stripe strategy led to higher residual tensile stresses, rationalized by longer scan paths, eventually promoting a more distinct thermal gradient. Especially the stresses parallel to the scan vectors increased with scan vector length and, thus, most significantly contributed to the stress state.[15] A reduction of stresses induced by short-track scanning was also highlighted for thin walls. Along the build direction, the stresses were found to alter from compressive stresses at the bottom to tensile stresses at the top.[16] Many studies investigated the influence of rotation in subsequent layers.[17] Here and in other studies, it was found that the strength and ductility are increased by a rotation of 90° in subsequent layers compared to unidirectional scanning.[18] These studies further revealed that rotational scanning can effectively reduce the tensile stresses at the top surface. Reduced stress by alternated scanning was found in other studies as well.[15] Many more characteristics of the process and material, respectively, can influence the final microstructure appearance. The processed material itself can undergo numerous phase transformations. In this case, the resulting phase composition has a major influence on the microstructural and mechanical properties.[19–21] Induced by the intrinsic heat treatment characteristic of AM processes, the evolution of an isotropic and fine-grained microstructure is possible. This has been revealed amongst others for a metastable austenitic CrMnNi steel recently.[22] In contrast, numerous materials not showing any phase transformation upon solidification and cooling tend to promote the evolution of strongly columnar, coarse-grained microstructures with strong <001> texture alongside the build direction, e.g., shown for stainless steel 316L and INCONEL 718 (IN718).[19,23–26]

In all studies, the high importance of thermal gradients and melt pool sizes is emphasized. A direct design of residual stresses seems possible through a good combination of processing parameters, including part geometry and scanning strategy. However, experimental evaluation of such considerations is hardly presented in the literature. Most importantly, the unique microstructures obtained upon AM pose tremendous challenges to the established techniques used to analyze residual stress. In most of the studies available, neither texture nor issues related to coarse grains are considered and assessed in depth. However, in conventionally manufactured materials, a strong influence of such aspects on evaluation of residual stresses has been reported.[27] Current challenges, limitations, and prospects arising in light of these considerations are detailed in Section 1.3.

1.2. Methods of Residual Stress Analysis

Generally, in engineering applications different methods are used to determine residual stresses in a component. These measuring methods are classified as destructive, semidestructive, and nondestructive measuring methods. Using nondestructive analysis methods, the residual stresses are determined by analyzing crystal lattice distortions of the materials in focus. The measurement of the crystal lattice deformation in a specific direction enables the calculation of residual stresses. Acoustic and magnetic measurement approaches are other techniques of nondestructive character. However, both methods have the

disadvantage that the final results strongly depend on the structural condition of the material, i.e., the contribution of microstructural characteristics other than residual stress is often significantly higher than the contribution of residual stress to the overall signals obtained.

(Semi-)Destructive analysis methods include the contour method and the hole-drilling (HD) method. These kind of analysis methods (mechanical methods) measure the macroscopic deformations resulting from a mechanical intervention (e.g., cutting or creating a borehole). These deformations are then used to evaluate the initial residual stresses. Often the measuring effort is relatively low.[28,29] However, extreme precision in the cutting or drilling process is required to analyze the residual stress states accurately.[27] It has been revealed that methods such as the HD technique are susceptible to errors in anisotropic structures, i.e., in case of calculation of residual stresses in components with textured and inhomogeneous anisotropic states.[27] A complex approach to solve the problem of an anisotropic textured state has been discussed in some studies.[27,29] Moreover, only the macroscopic residual stresses of the first type can be determined with this method. These issues clearly have to be critically assessed as even in conventionally manufactured components, residual stresses of the second type can reach absolute values of hundreds of megapascals.[30,31]

When residual stresses of the second type cannot be ruled out, more reliable results are obtained using diffraction methods.[28,29] Two methods are commonly used in laboratory environments for X-ray residual stress analysis (XSA): first, angle-dispersive (AD) diffraction using the characteristic radiation of the X-ray source, i.e., one wavelength only, and second, energy-dispersive (ED) diffraction based on white radiation.[28,32,33] In general, both approaches can be considered to be nondestructive; however, in the case of the layer-removal approach (very frequently used in AD-XSA), the technique changes to a semidestructive method. Focusing on ED-XSA, the multireflection of different crystal lattices can be measured simultaneously with an ED detector based on the white beam continuous characteristic.[32,33] Based on the white beam energy variation, the residual stress profile can be determined over a characteristic depth, i.e., the information depth (τ).[32] Both methods can be used to determine the residual stresses using the linear regression slope obtained over the variation of the measured crystal lattice spacing versus $\sin^2\psi$, where ψ is the inclination angle during the measurement. For this reason, knowledge of the X-ray diffraction elastic constants (DECs) of each hkl lattice plane is crucially necessary.[28,32]

The neutron and synchrotron diffraction techniques are also to be considered as nondestructive methods. Both are frequently used for the analysis of AM materials. The mentioned techniques, especially neutron diffraction, suffer from the disadvantage that they are not readily available for investigation. However, as major advantages, the high energy of radiation and the use of area detectors allow for the simultaneous detection and investigation of different crystal lattice reflections, eventually facilitating obtaining an overall picture of the residual stress states in the AM components at a fast data acquisition rate. In the case of both techniques, however, Hooke's approach is often used to calculate residual stress. In consequence, the

**ADVANCED
SCIENCE NEWS**

www.advancedsciencenews.com

**ADVANCED
ENGINEERING
MATERIALS**

www.aem-journal.com

knowledge of the exact unstressed lattice parameter (D_0) and the DEC is required.[31,34]

Obviously, all the methods, detailed previously, used for residual stress calculation have their advantages, limitations, and drawbacks.

To summarize at this point, the semi- and nondestructive methods based on X-ray diffraction can be used to determine the residual stresses of both the first and second type.[28,35] However, similar to the HD technique, these methods encounter limits with respect to the calculation of residual stresses with linear regression methods in the case of highly anisotropic and textured components. A comprehensive measurement approach has been discussed for conventionally processed materials to cope with these challenges.[28] The most critical issues related to the unique microstructural features of AM materials are highlighted in the following section.

1.3. Challenges for Diffraction Experiments

As mentioned previously, the microstructures of additively manufactured components vary significantly according to the manufacturing parameters and scan strategies applied.[25,36,37] The utilization of different AM systems, powder particle size distributions, or even overall component dimensions makes an individual adjustment of parameters necessary, in extreme cases differing for every individual component. The scan paths influence the thermal history of each part, just as parameters such as laser power and scan speed do, and need to be chosen carefully to prevent an early part failure due to porosities and residual stresses. Whereas the density of a part can be measured easily, by computed tomography (CT) or the Archimedes method, the reliable determination of residual stresses for a whole component is much more complex. A robust and reliable measurement method is needed to study the effects of scanning parameters on the residual stress states. AM components often have a textured microstructure due to a specific thermal history, which poses a challenge in terms of residual stress measurement.[38] Especially, cubic lattices tend to solidify in <100>-direction, resulting in a strong texture, while epitaxial growth at the same time leads to the evolution of microstructures being characterized by very large grain sizes.[23,25,39] Eventually, the reliability and applicability of the known residual stress analysis methods are detrimentally affected. Whereas the conventional $\sin^2\psi$-method can be readily applied for weak-textured, fine-grained samples, the highly textured, coarse-grained samples of IN718 cannot be reliably probed by this approach. For some specific conditions of AM microstructures, adapted or even new methods are under development. A method already has been proposed that is applicable for highly textured AM samples.[40] This method was shown to be relatively robust for assessment of materials characterized by pronounced anisotropy; however, it is not applicable in case of fine-grained or weakly textured samples. It is further sensitive to any additional local influence on texture (e.g., due to localized plastic deformation). Another drawback is the necessity of conducting a complete texture measurement in advance, which is not feasible during the measurements in transmission mode considered here. Thus, in light of the often ill-defined local texture state in AM samples, the best choice of the approach to be

considered remains vague. Only during or after conducting a measurement it can be assessed whether the selected method was an appropriate choice with respect to the accuracy of the residual stress calculations. With respect to the calculation of residual stresses from complete Debye–Scherrer rings (DSRs), so far the $\cos\alpha$ method and the direct method have been considered mainly focusing on the reflection mode.[41,42] In case of the $\cos\alpha$ method, the sample must be tilted to an appropriate angle (e.g., in the case of a Ni-base alloy 30° to the incoming beam) to determine the residual stress components σ_{11-33} and σ_{22-33}.[41] The direct method requires a powder distributed on the surface during measurement, eventually used to correct the recorded DSR (diffracted from the matrix) before residual stress calculation using mathematical algorithms can be accomplished.[42]

In contrast to the $\cos\alpha$ method introduced in the previous paragraph, for the novel method proposed, the beam is oriented normal to the sample surface, thus making the mathematical evaluation based on the standard equation of the $\cos\alpha$ method impossible. Furthermore, tilting the sample, especially in transmission mode, also distorts the irradiated gauge volume, eventually affecting the evaluation of the residual stress state. This kind of biasing factor can be avoided based on the novel approach detailed here.

By adapting the scan strategy during the production of the AM samples, the impact of texture on the residual stress measurements can be minimized, at least within the near-surface region.[43–45] Other issues encountered in XSA analysis of AM samples include surface roughness and internal flaws, such as porosity and lack of fusion, as addressed in several recent studies.[46–48]

In the case of laboratory measurements in reflection mode, the influence of such aspects is much more pronounced due to the lower information depth (penetration depth) of the beam and the resulting smaller gauge volume (e.g., depending on the wavelength of the beam, the angle of incidence, and the material under investigation). However, when measuring in transmission mode, where the sample is completely penetrated by the beam, the influence of any effects related to surface roughness can be neglected with respect to the information stemming from the remaining entire sample thickness.

In the present study, synchrotron diffraction measurements were performed on coarse-grained and weakly textured LPBF processed samples in transmission mode to introduce and validate the novel approach proposed. Principally, the novel method proposed is based on a linear regression approach, which is commonly applied in reflection mode. As in case of the $\sin^2\psi$-approach, phase-specific residual stresses and the sum of residual stresses of the first and second order can be experimentally determined using this approach. However, in present work the separation of the residual stress types was not considered further because the focus was on the assessment of the stability of the novel methodology. The novel method proposed is well applicable for larger sample thicknesses as long as in the thickness direction the attenuation of the X-ray beam is tolerable. In such a case, an average value describes the residual stress state of the sample well. In addition, the DSRs (being affected by grain morphology and texture) should be preferably more than 50% occupied, with a peak intensity ratio ($\frac{I^{max.}}{I^{background}}$) greater than 3. Considering these conditions, the residual stress gradient in

the thickness direction can be evaluated with a depth resolution in the submillimeter range, e.g., realized by using a conical slit cell mounted between the sample and the detector.[49]

To validate the applied method, in situ tensile tests were performed to investigate the stability of the experimentally determined strain distribution. Finally, based on the novel approach detailed, the local variation of residual stresses as a function of sample position and the influence of processing parameters were investigated for LPBF IN718.

2. Theory and Experimental Details

2.1. LPBF Sample Processing

The initial IN718 powder, supplied by VDM Metals, was characterized by a particle size distribution between 20 and 63 μm. The chemical composition of the powder was in the standard range of IN718. Thin-wall samples and samples for the in situ tensile tests were produced using an SLM280HL machine from SLM Solutions GmbH (Lübeck, Germany). Although the system is equipped with two different laser sources, for sample production only the laser with a nominal power of 400 W and a Gaussian beam profile was used. The laser power used for processing

the IN718 was 250 W with a scan speed of 850 mm s^{-1}. The layer thickness was 0.04 mm, and the hatch distance 0.1 mm. All samples with a size of $20 \times 40 \times 1$ mm^3 were manufactured with a substrate heating to 200 °C. For the samples, a bidirectional (Bi-Di) scanning was considered, where the scan direction was rotated in every successive layer with an angle of 90° (see **Figure 1**).

For tensile testing (Section 2.3), flat samples with dimensions of $34 \times 1.6 \times 1.5$ mm^3 were cut by electrodischarge machining (EDM) (see **Figure 2**a) from a 100Cr6 block (dimensions of $50 \times 50 \times 20$ mm^3) and the LPBF IN718 blocks (dimensions of $20 \times 25 \times 40$ mm^3). The 100Cr6 was characterized by a fine-grained, "fine lamellar" state due to the heat treatment conducted, while the LPBF IN718 blocks were additively manufactured using the strategy with 90° rotation between each layer. The same laser power was used as in case of the thin-wall samples (Figure 1a). Stress-relieving heat treatment was performed on the 100Cr6 samples before tensile testing to remove any residual stresses due to machining. Because there is no recommendation for stress-relieving or stress-equalization as heat treatment of IN718 according to the *ASM Handbook*, Volume 4, the sample was subjected to soft annealing in the δ-phase region (960 °C, 1 h, air-cooled).[50,51] All tensile test samples were loaded uniaxially during the synchrotron measurement.
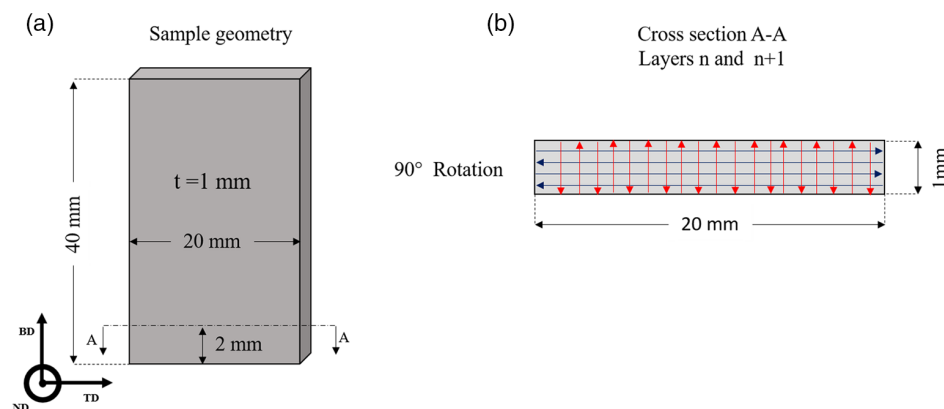
Figure 1. Sample geometry and scan strategy used in this work: a) schematic illustration of the sample and b) the Bi-Di scan strategy with 90° rotation depicted for cross-section A-A, 2 mm distance to the build platform.
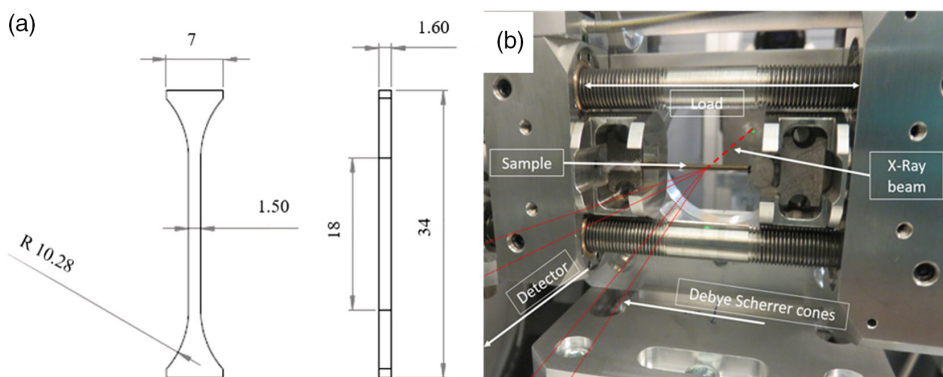
Figure 2. a) The geometry of the flat tensile sample and b) the testing setup including the miniature stress rig. All dimensions in millimeter.

2100184 (4 of 15)

2.2. Measurement Methods for Residual Stresses Based on X-ray Diffraction Experiments including the Novel Approach

To calculate residual stresses from experimentally determined strains related to several lattice planes, the well-known Equation (1) based on Hooke's law (considering relevant sample and measurement coordinate transformations) is most commonly used.[28]

$$
\begin{aligned}
\varepsilon_{\varphi,\psi}^{\{hkl\}} = {} & \frac{1}{2} s_2^{\{hkl\}} (\sigma_{11}\cos^2\varphi\sin^2\psi + \sigma_{22}\sin^2\varphi\sin^2\psi + \sigma_{33}\cos^2\psi) \\
& + \frac{1}{2} s_2^{\{hkl\}} (\sigma_{12}\sin(2\varphi)\sin^2\psi + \sigma_{13}\cos\varphi\sin(2\psi) \\
& + \sigma_{23}\sin\varphi\sin(2\psi)) + s_1^{\{hkl\}}(\sigma_{11} + \sigma_{22} + \sigma_{33})
\end{aligned}
\tag{1}
$$

Here, $\frac{1}{2}s_2^{\{hkl\}}$ and $s_1^{\{hkl\}}$ are the already mentioned DECs and φ, ψ are the azimuth and tilting angle, respectively.[52] Appropriate DEC values usually are determined from measurements on single crystals (or direct measurement considering fine-grained samples under load). From these tests, DEC values are approximated based on different approaches, such as Reuss, Voigt, and Hill.[28,35,52] In the case of these approaches, the same material and the respective {hkl} have to be considered. For a coarse-grained microstructure characterized by weak texture, the coarse grain effect can be reduced by increasing the diffracting gauge volume. Thus, the use of DEC values similar to the $\sin^2\psi$ approach is thought to be possible. Thus, experimental determination of DEC values has been refrained from in this work.

In the following, the concepts used for the development of the novel formalism proposed in this work are described in detail.

2.2.1. Generalized Hooke's Equation

Generally, Hooke's law assumes that a direct proportionality between deformation and loading force in the elastic region prevails, especially in isotropic materials. This proportionality is considered the physical property of the loaded material.[52] The area detector offers the possibility to detect the necessary reflection in a particular direction, i.e., $\alpha = 0°, 90°, 180°$, and $270°$, in a fully occupied DSR. By applying the following generalized Hooke's equation (Equation (2)); the residual stresses in these directions can be calculated[28]

$$
\sigma_{ij}^{\{hkl\}} = \frac{1}{\frac{1}{2}s_2^{\{hkl\}}} \left[\varepsilon_{ij}^{\{hkl\}} - \delta_{ij}\frac{s_1^{\{hkl\}}}{\frac{1}{2}s_2^{\{hkl\}} + 3s_1^{\{hkl\}}}(\varepsilon_{11} + \varepsilon_{22} + \varepsilon_{33}) \right]
\tag{2}
$$

where the following is to be considered

$$
\delta_{ij} = \begin{cases} 1 \text{ if } i = j \\ \text{and} \\ 0 \text{ if } i \neq j \end{cases}
\tag{3}
$$

To calculate ε_{ij}, the Equation (4) (a simplified version of Equation (1)) and the well-known Bragg's equation[28] are used, where $\varepsilon_{ij}^{\{hkl\}}$ is set to be either 11, 22, or 33.

$$
\varepsilon_{ij}^{\{hkl\}} = \frac{\sin\theta_0^{\{hkl\}} - \sin\theta_{ij}^{\{hkl\}}}{\sin\theta_{ij}^{\{hkl\}}}
\tag{4}
$$

Based on the measurement in transmission mode and for the simplification of the calculation, it is assumed that $\varepsilon_{33} = 0$, which is not always fulfilled and may influence the results. The sample and detector coordinate system must comply with each other. In addition, it has to be mentioned that all values of $\varepsilon_{ij}^{\{hkl\}}, \sigma_{ij}^{\{hkl\}}$ (Equation (2) and (4)) must be calculated separately for the main sample directions, i.e., the mean value of the calculated strains in the direction of $\alpha = 0°$ and $180°$ for the build direction (BD), and $\alpha = 90°$ and $270°$ for the transversal direction (TD).

As mentioned in the introduction, the calculation of residual stresses with this approach is highly dependent on the exact value of the stress-free crystal lattice parameter, i.e., $\theta_0^{\{hkl\}}$ or $D_0^{\{hkl\}}$. In the literature, an accuracy of 10^{-5} is recommended, if the $D_0^{\{hkl\}}$ has to be used directly for the calculation of the residual stresses.[35] For determining these absolute values, commonly, the measurements are performed on a stress-free calibration powder with the same chemical composition and heat treatment in case of the investigated sample. However, for AM samples, calibration powders that meet the requirements are not easily accessible. For example, according to the standard EN13925-2, the calibration powder grains should be uniformly sized (less than 10 μm), randomly textured, stress-free, and have the same chemical composition as the sample of interest to meet the requirements for X-ray $D_0^{\{hkl\}}$ determination. However, the size of the used powders in AM sample production is not uniform, varying from 20 to 60 μm. Moreover, due to the potential alloying element vaporization during AM sample processing,[53,54] different chemical compositions along one sample may be present. In addition to the application of powder measurement for the determination of $D_0^{\{hkl\}}$, alternative approaches, including their limitations, were already discussed in the literature.[54,55]

As a result, the use of this approach for AM samples will not always yield the correct residual stress value in a robust fashion.

By applying all the considerations mentioned before and based on Equation (2) and (4), Equation (5) can be derived as follows

$$
\sigma_{11-33}^{\{hkl\}} = \frac{\varepsilon_{11}^{\{hkl\}} - \varepsilon_{33}^{\{hkl\}}}{\frac{1}{2}s_2^{\{hkl\}}} = \sigma_{11}^{\{hkl\}} - \sigma_{33}^{\{hkl\}}
\tag{5}
$$

Based on Equation (5), residual stress $\sigma_{11-33}^{\{hkl\}}$ can be calculated in a similar way as in XSA in reflection mode. Most importantly, the necessity of knowing the exact value of the stress-free crystal lattice parameter can be avoided.

2.2.2. Sin²ψ Approach

The $\sin^2\psi$ approach in reflection mode is a well-known method for the calculation of the residual stress $\sigma_{11-33}^{\{hkl\}}$ based on a linear regression model. This approach is usually used in reflection mode, where due to the lower energy of the beam, the penetration depth and gauge volume are relatively small. However, this can be regarded as a drawback in the case of residual stress
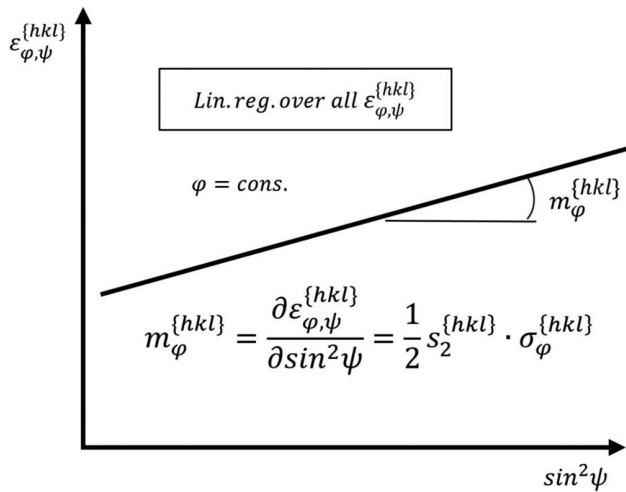
Figure 3. Strain distribution over $\sin^2\psi$ at constant azimuth angle φ.

analysis in AM materials, especially for textured and coarse-grained samples being characterized by nonadequate grain statistics in the gauge volume.

The values $\varepsilon_{\varphi,\psi}$ in the fundamental equation of the XSA (Equation (6)) are a simplification of Equation (1) by neglecting shear stresses, eventually representing the lattice strains determined in the directions φ, ψ, where φ, ψ are the azimuth and tilting angle, respectively.[28]

$$\varepsilon_{\varphi,\psi} = \frac{D_{\varphi,\psi}^{\{hkl\}} - D_0^{\{hkl\}}}{D_0^{\{hkl\}}} = \varepsilon_{11}\cos^2\varphi\sin^2\psi + \varepsilon_{22}\sin^2\varphi\sin^2\psi + \varepsilon_{33}\cos^2\psi \quad (6)$$

Figure 3 shows the strain distribution, $\varepsilon_{\varphi,\psi}$, for a constant azimuth angle φ in a plane stress state over $\sin^2\psi$.

The residual stresses have direct proportionality to the slope of the linear regression $m_\varphi^{\{hkl\}}$ as shown in Equation (7), and therefore can be determined straightforward

$$m_\varphi^{\{hkl\}} = \frac{\partial \varepsilon_{\varphi,\psi}^{\{hkl\}}}{\partial \sin^2\psi} = \frac{1}{2}s_2^{\{hkl\}}\sigma_\varphi^{\{hkl\}} \quad (7)$$

The $\sin^2\psi$ approach, in contrast to Hooke's approach, has the advantage of simplicity of application. In this case, for the calculation of residual stresses only one DEC, i.e., $\frac{1}{2}s_2^{\{hkl\}}$, is sufficient.[28] Moreover, in the $\sin^2\psi$ approach, using $m_\varphi^{\{hkl\}}$ for the residual stress calculation, the dependence on the exact value of $\theta_0^{\{hkl\}}$ or $D_0^{\{hkl\}}$ is negligible as the induced error due to the inaccurate stress-free crystal parameter only shifts all the calculated data to the same extent and, thus, does not affect the slope of the regression, the latter being the characteristic value related to the residual stress state. These advantages are also accomplished by the adapted Hooke's approach (Equation (5)). Nevertheless, the main advantage of the $\sin^2\psi$ approach is its robustness against data scattering by considering data obtained at numerous sample tilting angles.

2.2.3. Sin²α Approach

The proposed $\sin^2\alpha$ approach can be used in transmission mode residual stress analysis. Here, the residual stress $\sigma_{11-33}^{\{hkl\}}$ is calculated through linear regression, similar to the $\sin^2\psi$ approach in reflection mode.

Using an area detector, the $\sin^2\alpha$ approach incorporates the advantage of capturing the full DSR. This implies that the crystal lattice diffraction data of the respective DSR can be used to determine the residual stresses based on the linear regression method.

For this purpose, the transmission mode measurement configuration is defined as highlighted in **Figure 4**.
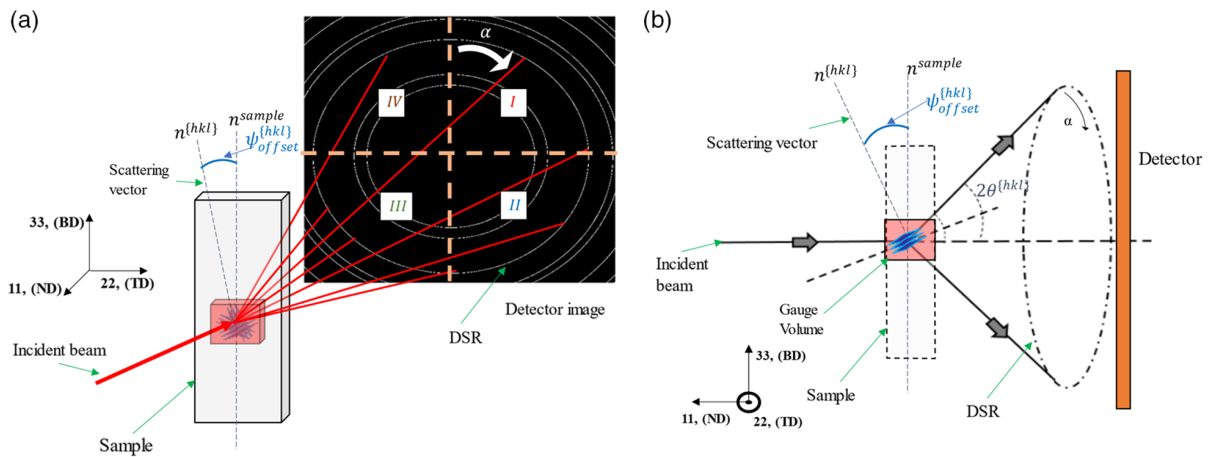
Figure 4. Schematic representation of the measurement configuration in case of the $\sin^2\alpha$ approach in transmission mode in a) front view and b) side view; in both schematics, the incoming beam is oriented perpendicular to the sample surface and the beam fully penetrates the sample. The red box represents the gauge volume and the blue lines represent the diffracting crystal lattices; the ψ_{offset} represents the angle between the normal to the surface, $\mathbf{n}^{Sample}$, and the crystal lattice scattering vector $\mathbf{n}^{\{hkl\}}$. In (a), each quarter of the detector is labeled with roman letters, I, II, III, and IV, where the starting angle, $\alpha = 0°$, and its direction are highlighted on the detector image by the white arrow.

Table 1. Angles between the orthonormal vector to the crystal plane and the normal to the sample surface $\psi_{offset}^{\{hkl\}}$ for seven different lattice planes of ferrite.

hkl	110	200	211	220	310	222	321
$2\theta_0^{\{hkl\}}$ (deg)	4.02	5.69	6.97	8.05	9.01	9.87	10.66
$\psi_{\text{offset}}^{\{hkl\}}$ (deg)	2.01	2.85	3.49	4.03	4.50	4.93	5.33

Similar to the Hooke's-approach an $\psi_{offset}^{\{hkl\}}$ prevails. In transmission mode, this offset is equal to $\frac{2\theta_0^{\{hkl\}}}{2}$. Obviously, this offset can influence the calculated results. However, due to the high–energy synchrotron radiation, the $2\theta_0^{\{hkl\}}$ of all diffraction interferences are small. As a result, the influence of this offset on the determined residual stresses is thought to be negligible. **Table 1** shows $\psi_{offset}^{\{hkl\}}$ and $2\theta_0^{\{hkl\}}$ for the synchrotron energy of 87.1 keV calculated for the α-ferrite phase of steel.

By taking the $\varepsilon_\alpha^{\{hkl\}}$ of each DSR quarter and forming a linear regression over $\sin^2\alpha$ (**Figure 5**), the residual stress difference can be calculated using Equation (8).

$$m^{\{hkl\}} = \frac{\partial \epsilon_\alpha^{\{hkl\}}}{\partial \sin^2\alpha} = \frac{1}{2} s_2^{\{hkl\}} \sigma_{22-33}^{\{hkl\}} = -\frac{1}{2} s_2^{\{hkl\}} \sigma_{33-22}^{\{hkl\}} \qquad (8)$$

In the equation $m^{\{hkl\}}$ is the slope of the linear regression line over $\varepsilon_\alpha^{\{hkl\}}$–$\sin^2\alpha$. As the main difference to Hooke's approach, of the linear regression over all quarters minimizes the influence of the detector calibration, including the detector tilt effect, the detrimental effects of texture and coarse grains, and eventually effects related to statistics in general. It can also be assumed that in transmission mode, due to the equilibrium condition of the residual stresses, the macroscopic residual stresses of the first type in the thickness direction will be equal to zero. Furthermore, it is important to note that in present work only the residual stresses of the matrix phase are analyzed.
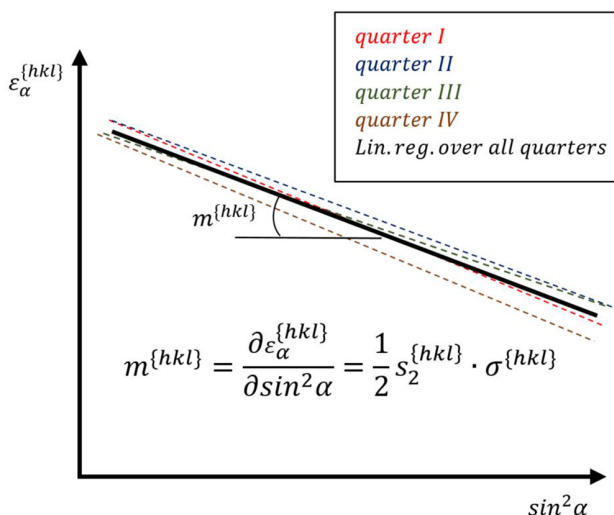
Figure 5. Strain distribution over $\sin^2\alpha$.

2.3. Setup, Measurement Conditions, and Data Processing

For the experimental validation of the methods, in situ tensile tests were performed at the beamline P02.1 at DESY (Deutsches Elektronen-Synchrotron, Hamburg, Germany).[56] Synchrotron radiation energy of ≈59.8 keV was applied in an in situ approach using a miniature stress rig (Kammrath&Weiss, Figure 2b) focusing on two fundamentally different materials: a conventionally manufactured 100Cr6 steel that already had been studied in depth before,[57,58] and LPBF processed IN718 (see Section 2.1). The former was studied to validate the applicability of the novel approach, and the latter was used to assess the reliability and robustness of the approach for characterization of weakly textured, coarse-grained material. Prior to residual stress analysis, the detector measurements were calibrated using an LaB6 standard as well as a Python-based tool, named "pyFAI."[59,60] This program was also used in a Python script for azimuthal integration (caking) with a step size of 2° and a nominal radial resolution of 0.015°. For importing the TIFF images in Python, FabIO was used.[61] For the calculation of residual stresses in MATLAB following both approaches considered the median of all $\theta_\alpha^{\{hkl\}}$ of each DSR was taken as $\theta_0^{\{hkl\}}$ (stress-free diffraction angle) from the first image. This step is thought to be absolutely reasonable due to the prior heat treatment eventually minimizing the resulting error when using Hooke's approach. Moreover, any influence of variation of composition on the results can be neglected here as all measurements were always performed on a single measurement point (MP).

After initial data analysis, both approaches were applied to the in situ tensile test data, and all residual stress values were subtracted by the mean stress values calculated from the first ten images. This step provided a robust basis for meaningful comparison of the values taken from the tensile testing machine with the values calculated from the diffraction patterns.

Finally, synchrotron measurements of LPBF processed IN718 samples were performed at HZG beamline P07–EH1 station (Petra III, DESY) in transmission mode.[62] The energy of 87.1 keV and a Perkin Elmer XRD 1621 area detector (with 2048 × 2048 pixels, size of 200 × 200 μm² each) were used for all measurements. The beam dimensions for the space-resolved mapping were set to 0.5 × 0.5 mm². For the area detector image analysis, the same procedure was performed as described for the in situ tensile tests (including data from simulated conditions to correct the detector tilt effect and allow for an adequate peak fit). Subsequently, the residual stresses were calculated using the $\sin^2\alpha$ approach proposed here. The synchrotron beam and the area detector enable the simultaneous detection of the DSR of different crystal lattice planes and eventually allow for efficient residual stress mapping. For the residual stress mapping, 200 measurement points were defined on each LPBF IN718 sample surface. The measurement points near the sample edges were set at a distance of 1 mm from each edge; the distance between adjacent points was set to 2 mm. The measurement procedure was highly automated so that after alignment of the sample and defining the sample edges, a script was executed moving the sample perpendicular to the incident beam in 2 mm steps horizontally and vertically. The time for acquiring a single image at each measurement point was set to 0.1 s. Still, the overall measurement time

of one sample yielded about 30 min, the total elapsed time mainly caused by sample movement. For illustrative purposes, the results were plotted using the MATLAB function *contourf*.

Microstructure analysis was conducted using a Zeiss ULTRA GEMINI high-resolution SEM operating at 20 kV. The SEM system is equipped with an electron backscatter diffraction (EBSD) unit. For EBSD measurements, all samples were mechanically ground to 5 µm grit size using SiC paper and then vibration polished for 12 h using a conventional oxide polishing suspension (OPS) with a grain size of 0.04 µm. All measurements were performed using the same working distance, magnification, and step size, i.e., 14 mm, 200×, and 0.5 µm. Postprocessing of EBSD data sets was conducted using the Bruker ESPRIT software.

3. Results and Discussion

3.1. Microstructure of the Investigated Samples

Figure 6 shows an example of the microstructural characteristics of a single LPBF IN718 sample processed using the Bi-Di scan strategy and 90° rotation, where a slightly preferred grain orientation with the <001> alongside BD can be seen (Figure 6b). The EBSD analysis was performed at a distance of about 150 µm (in the depth direction [ND]) to the sample surface.

Furthermore, grains are relatively coarse (Figure 6b). The EBSD micrograph shows an inverse pole figure (IPF) map colored according to the standard triangle (shown as an inset to Figure 6). Grains and clusters of grains of virtually the same orientation with respect to the BD are seen, where individual grains are characterized by a diameter of around 50 µm. In contrast to data shown in the literature for IN718,[24] however, no notable grain elongation alongside the BD is resolved due to the plane of view depicted. This coarse-grained, anisotropic microstructure leads to ill-defined DSRs (Figure 6c) as indicated by the high variation of intensities alongside every individual ring (Figure 6d). This observation holds true even at beam sizes of $1 \times 1 \, mm^2$.

Whereas the pronounced texture affects the detector images in the same way across the entire sample surface, the effect of the coarse microstructure is different for each detector image and, thus, hinders straightforward determination of residual stresses. This effect is even more pronounced when characterization under lab conditions in reflection geometry is considered due to the more limited gauge volume. By increasing the gauge volume to the entire sample thickness in transmission mode at high X-ray energies using synchrotron radiation, the grain statistics can be significantly improved. Thus, residual stress analysis was thought to be possible even considering the prevalent microstructure. The following sections prove that the novel approach proposed is well suited for robust analysis of residual stress for such kinds of microstructures. Based on simulations and experiments, data are assessed and validated.

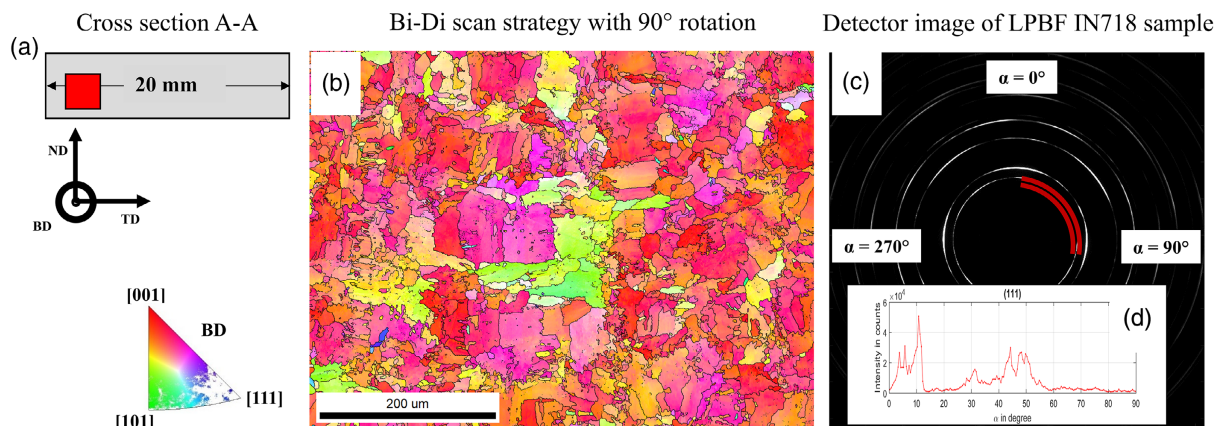### 3.2. Residual Stress Analysis by Hooke's Law and $Sin^2\alpha$ Approach in Simulation

The simulation was performed step by step as described in the following to verify the applicability of the methods introduced here. At the end of this section, a calculated detector image is shown. This data set is then used for experimental validation. Afterwards, the analysis protocol is applied for determining the residual stresses in the LPBF IN718 samples.

For the simulation, the parameters of ferritic steel with a lattice spacing of $a_0 = 0.28665$ nm were used, and an energy of 87.1 keV was chosen to represent the synchrotron radiation (in line with the used energy at the HZG beamline P07–EH1, DESY, Hamburg). Furthermore, the sample-to-detector distance (SDD) was set to 734 mm.

In the next step, a triaxial residual stress state was defined, with residual stress components that could be randomly chosen. Equation (9) was used to calculate the strain variations.[28]

$$\varepsilon_\alpha^{hkl} = \frac{1}{2} s_2^{\{hkl\}}(\sigma_{11}n_1^2 + \sigma_{22}n_2^2 + \sigma_{33}n_3^2 + 2\tau_{23}n_2n_3 + 2\tau_{31}n_3n_1 + 2\tau_{12}n_1n_2) + s_1^{\{hkl\}}(\sigma_{11} + \sigma_{22} + \sigma_{33}) \quad (9)$$

where the components of the rotated scattering vector n_1, n_2, and n_3 (according to the definitions for the $\cos\alpha$ approach in reflection mode, e.g., in Tanaka[41]) were used to obtain a complete DSR.

| Cross section A-A | Bi-Di scan strategy with 90° rotation | Detector image of LPBF IN718 sample |

Figure 6. a) Schematic A–A cross-section of the LPBF IN718 sample, see also Figure 1a; b) EBSD IPF map; c) a detector image acquired at 2 mm distance from the build platform (HZG, P07) where the intensity distribution for the 111-lattice plane in the red-dotted section is plotted in (d). The red box in (a) indicates the location of volumes probed by EBSD.

**ADVANCED
SCIENCE NEWS**

www.advancedsciencenews.com

**ADVANCED
ENGINEERING
MATERIALS**

www.aem-journal.com

$$n_1 = \sin\theta_0 \tag{10}$$

$$n_2 = \cos\theta_0 \sin\alpha \tag{11}$$

$$n_3 = \cos\theta_0 \cos\alpha \tag{12}$$

For the simulation with respect to the transmission mode, α angles varied from 0° to 360° and the $\theta_0^{\{hkl\}}$ angle (Table 1) was calculated for each DSR as follows

$$\theta_0^{\{hkl\}} = \sin^{-1}\left(\frac{\lambda\sqrt{h^2 + k^2 + l^2}}{2a_0}\right) \tag{13}$$

Afterwards, the calculated strains were transformed into $2\theta_\alpha^{\{hkl\}}$ using Equation (14) and (15)[28,35]

$$D_\alpha^{\{hkl\}} = D_0^{\{hkl\}} \cdot (\varepsilon_\alpha^{\{hkl\}} + 1) \tag{14}$$

$$\theta_\alpha^{\{hkl\}} = \sin^{-1}\left(\frac{\lambda}{2D_\alpha^{\{hkl\}}}\right) \tag{15}$$

Taking the predefined pixel size and SDD in micrometers, in this step, the respective radii on the detector in pixels can be calculated by the following equation (Equation (16))[41]

$$r_\alpha^{\{hkl\}} = \frac{\text{SDD} \cdot \tan 2\theta_\alpha^{\{hkl\}}}{\text{pixel size}} \tag{16}$$

To simulate an area detector image similar to the one used, i.e., an area detector Perkin Elmer XRD 1621, a matrix with 2048 × 2048 elements was defined, and the center was set to $[x_{\text{center}}, y_{\text{center}}] = [1024, 1024]$. Using Equation (17) and (18), the polar coordinate system was transferred to the Cartesian coordinate system (for details, see, e.g., He[34]).

$$x_\alpha^{\{hkl\}} = x_{\text{center}} + r_\alpha^{\{hkl\}} \cdot \cos\alpha \tag{17}$$

$$y_\alpha^{\{hkl\}} = y_{\text{center}} + r_\alpha^{\{hkl\}} \cdot \sin\alpha \tag{18}$$

After rounding the obtained pairs of $x_\alpha^{\{hkl\}}$ and $y_\alpha^{\{hkl\}}$, an intensity of 1000 counts was allocated to each pair. As a result, a matrix of third order was created (x and y positions on the detector image and intensity). Finally, the matrix was saved as an image in the ".TIFF" format (**Figure 7**).
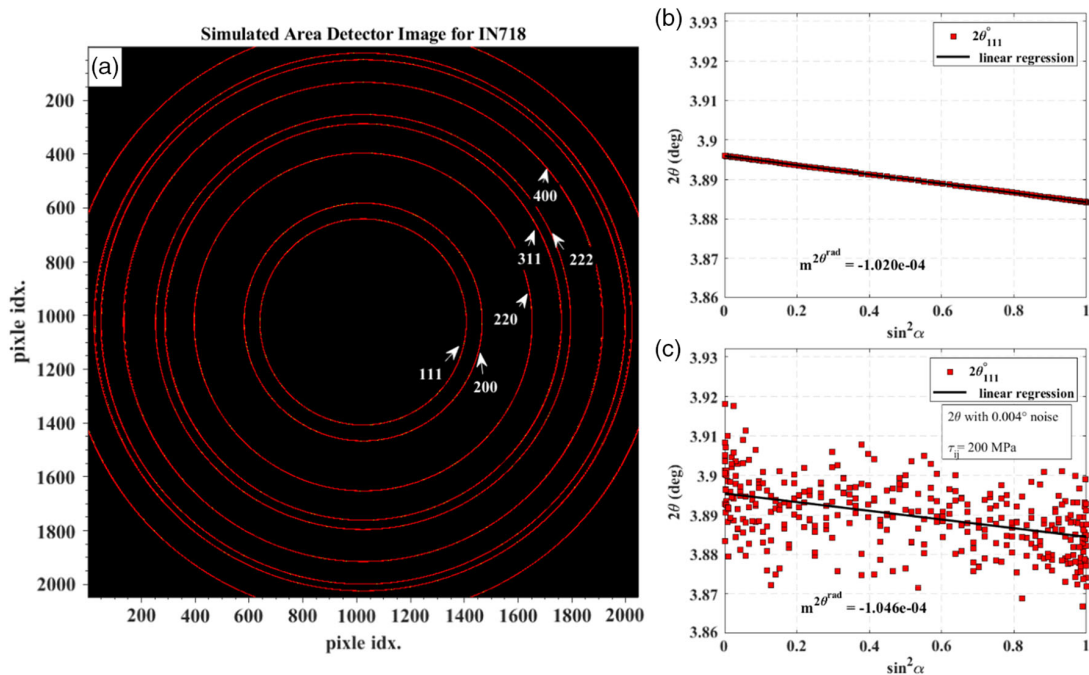
The simulated area detector image was used as a reference in the analysis program (written in MATLAB) to directly compare the output with the residual stress inputs. Finally, this program was used to analyze all experimental data obtained.

After determining and indexing of $2\theta_\alpha^{\{hkl\}}$ for each DSR, residual stresses were calculated using Equation (8).

For the evaluation of residual stresses in LPBF IN718 samples in this study, the DEC values according to the Reuss approach were used (**Table 2**) as recommended in previous studies.[44,45]

Figure 8 shows the results calculated using the $\sin^2\alpha$ approach and Hooke's equation, respectively, for the selected values $\sigma_{22} = 800$ MPa, $\sigma_{33} = 100$ MPa, and $\sigma_{11} = 50$ MPa.

It is important to note that all shear stresses $\tau_{ij}^{\{hkl\}}$ were set to 0 MPa. Based on these sets of data, both methods should yield $\sigma_{22-33} = 700$ MPa.

Figure 7. a) Representative example of the simulated area detector image for IN718 with an energy of 87.7 keV and an SDD = 1123 mm. The first six lattice planes were identified (white numbers); b) $2\theta_{111}^\circ - \sin^2\alpha$ course for the case without noise and $\sigma_{\text{BD-TD}} = 700$ MPa, the calculated slope is $m^{2\theta^{\text{rad}}} \cong -1.020 \times 10^{-4}$; c) The same diagram with 0.004° noise over $2\theta_{111}^\circ$, and $\tau_{ij} = 200$ MPa, the calculated slope is $m^{2\theta^{\text{rad}}} \cong -1.046 \times 10^{-4}$.

Table 2. DEC values according to the Reuss approach used in the present work.

Material	$\{hkl\}$	s_1 [Pa^{-1}]	$\frac{1}{2}s_2$ [Pa^{-1}]
100Cr6	110	−1.27	5.8
	200	−1.9	7.7
	211	−1.27	5.8
	220	−1.27	5.8
	310	−1.67	7.02
LPBF-IN718	111	−8.4	4.31
	200	−2.91	7.53
	220	−1.35	5.86
	311	−1.93	7.6
	222	−8.4	4.31
	400	−2.91	7.53

Both methods yield relatively correct values for the calculated residual stress from different DSRs of different lattice planes. However, the absolute values obtained exhibit a minor deviation (max. 10 MPa) from the set values (700 MPa), which is due to the aforementioned influence of the $\psi_{\text{offset}}^{\{hkl\}}$ value, which increases as the $2\theta^{\{hkl\}}$ increases.

To simulate a more realistic case, like in the case of coarse-grained, anisotropic AM samples, the $2\theta_\alpha^{\{hkl\}}$ were randomly noised by 0.004°. Such a value is in good agreement to a noise level resulting, e.g., from insufficient irradiation time, detector inaccuracy, or sample-related characteristics such as unfavorable grain morphology, texture, and ill-defined sample thickness. Furthermore, the possible detector tilt leading to distortion of the DSR was simulated by defining shear stress components of $\tau_{12}^{\{hkl\}} = \tau_{13}^{\{hkl\}} = \tau_{23}^{\{hkl\}} = 200\,\text{MPa}$.

The principal residual stresses remained the same as in the previous case. The results obtained by the $\sin^2\alpha$ approach (**Figure 9**a) represent a much better fit to the target value (700 MPa) than the results obtained from Hooke's approach (Figure 9b).

For each lattice plane, the standard deviation of ten consecutive simulation results is given in form of error bars. For the

simulation case without noise, all errors were equal to zero. However, in the case of 0.004° random noise over 2θ, the results of both approaches exhibit obvious deviations. In this case, significant scatter for the Hooke's approach results are seen.

For the case that the stresses in the thickness direction are not in an equilibrium state, e.g., during a tensile test, $\sigma_{11,\text{ND}}$ in the simulation was set to 400 MPa. In such a case, an absolute residual stress value variation of less than 2 MPa was observed for each lattice plane.

It has to be noted that the influence of this scattering is maybe even more significant in the case of real measurements.

3.3. Validation of the Proposed Novel Approach by In Situ Experiments

For validation of the novel approach, in situ tensile tests were conducted for the reference material and the material in the focus of this work, i.e., 100Cr6 and LPBF IN718. For both materials, detector images were analyzed using the $\sin^2\alpha$ approach and Hooke's approach. The loading stresses versus calculated, measured stresses are shown in **Figure 10** and **11**, respectively. The results of the linear regression of these curves are given in **Table 3**. Furthermore, the fit parameters and quality values of linear regression for each curve are listed in Table 3. For both materials, detector images were calculated by the $\sin^2\alpha$ approach and Hooke's approach. As can be seen, the calculated residual stresses obtained by both methods correlate well with the loading stresses in the case of the 100Cr6 reference material. This holds for stress-relieved posttreated LPBF IN718 at relatively low absolute values of stress as well. However, it can be seen that at the high loading stress level, the calculated residual stress values in case of some lattice planes deviate significantly from the loading stress values. This can be attributed to both the $\psi_{\text{offset}}^{\{hkl\}}$ and the possible local onset of plastic deformation in the samples. Furthermore, as shown in Figure 10a, the calculated stresses start to deviate from the values of the loading stresses by ≈10 MPa when the load stress equals 50 MPa. This deviation increases continuously to about 50 MPa when the loading stress reaches 300 MPa. Due to the lateral contraction, stresses are
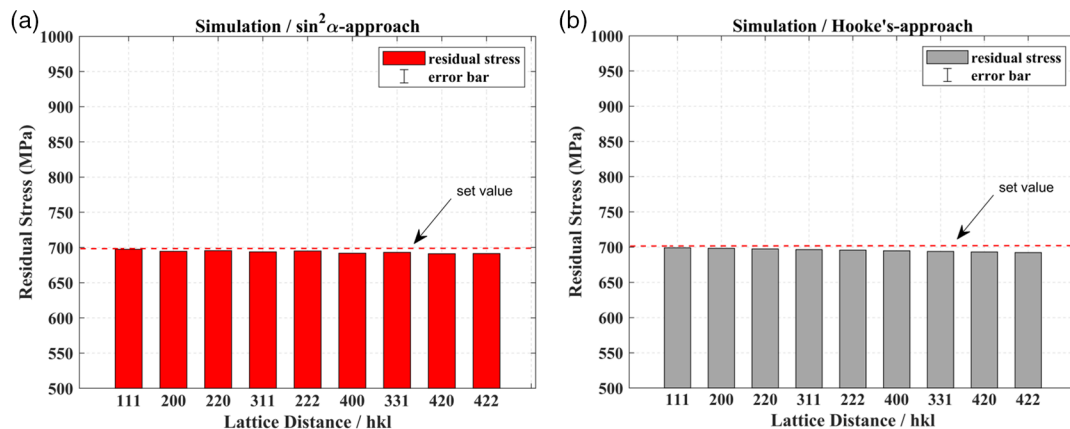

Figure 8. Calculated residual stress values based on simulated data for IN718, matrix phase applying a) $\sin^2\alpha$ approach and b) Hooke's-approach; errors are equal to zero.
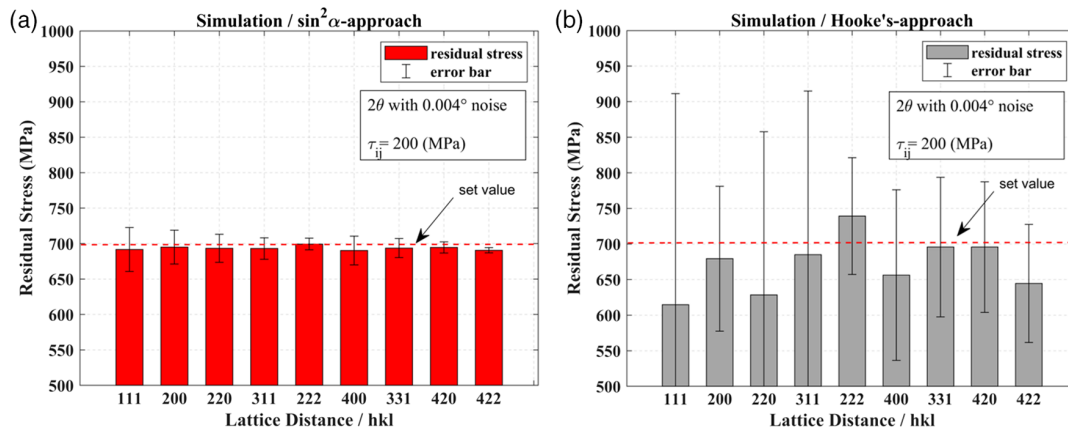
Figure 9. Calculated residual stress values for IN718 and matrix phase taking into account simulated data with 0.004° noise in 2θ values and $\tau_{12}^{\{hkl\}} = \tau_{13}^{\{hkl\}} = \tau_{23}^{\{hkl\}} = 200$ MPa applying a) $\sin^2\alpha$ approach and b) Hooke's-approach.
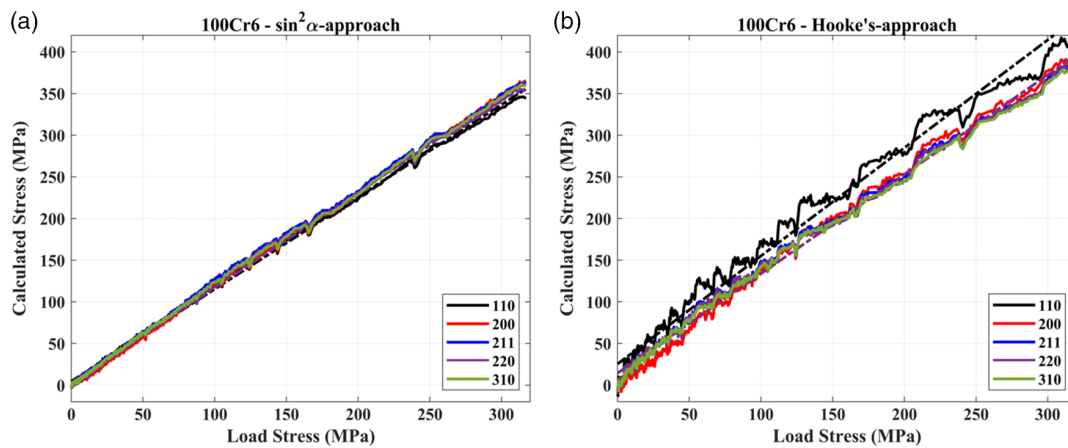
Figure 10. Tensile test results for the 100Cr6 sample: stresses calculated by a) $\sin^2\alpha$ approach and b) Hooke's approach, respectively. Linear regression lines are shown for lattice planes 110 and 220 by dotted lines.
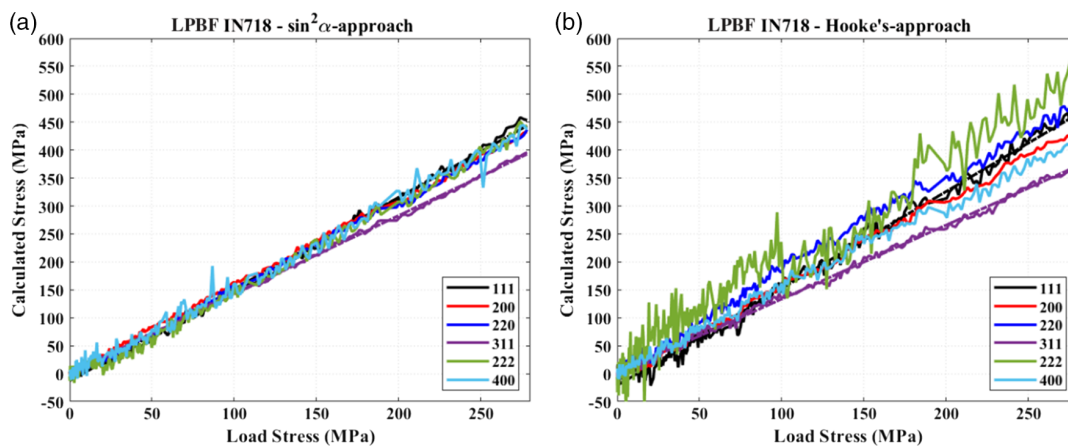
Figure 11. Tensile test results for the LPBF IN718 sample: stresses calculated by a) $\sin^2\alpha$ approach and b) Hooke's approach, respectively. Linear regression lines are shown for lattice planes 111 and 311 by dotted lines.

2100184 (11 of 15)

ADVANCED
SCIENCE NEWS
www.advancedsciencenews.com

ADVANCED
ENGINEERING
MATERIALS
www.aem-journal.com

Table 3. Parameters m and b (in MPa) obtained by linear regression of calculated stresses versus load stresses upon applying $\sin^2\alpha$ approach and Hooke's approach for 100Cr6 and LPBF IN718 (including parameters indicating the quality of fit: R^2, mean square error (MSE) in MPa^2).

Material	Lattice plane	Sin²α approach				Hooke's approach			
		m	b	R^2	MSE	m	b	R^2	MSE
100Cr6	110	1.1070	4.607	0.9987	12.7832	1.2970	25.38	0.9841	210.650
	200	1.1683	−0.822	0.9993	7.4038	1.2732	2.524	0.9959	51.5844
	211	1.1575	4.534	0.9987	13.7078	1.1985	15.16	0.9937	70.6420
	220	1.1464	2.321	0.9986	14.2206	1.1936	14.32	0.9946	60.0043
	310	1.1505	3.011	0.9991	9.7235	1.1910	12.92	0.9948	57.2891
LPBF IN718	111	1.6416	−12.81	0.9959	73.0649	1.7354	−21.09	0.9919	162.651
	200	1.5422	3.098	0.9990	16.3265	1.5922	−6.397	0.9976	40.4307
	220	1.5591	−5.093	0.9988	19.4563	1.7411	4.992	0.9943	114.044
	311	1.4085	1.168	0.9994	8.4808	1.3238	1.149	0.9969	36.4932
	222	1.5972	−12.46	0.9935	109.486	1.8223	15.56	0.9492	1174.18
	400	1.5674	−2.375	0.9908	149.116	1.4865	3.859	0.9940	88.6814

present transversely and in thickness direction in the tensile test. Obviously, stresses induced by tensile testing are, in contrast to the residual stresses, not in a state of equilibrium; therefore, on one hand, the sum of the stresses in the thickness direction is not zero and, on the other hand, as the presented method calculates the $\sigma_{\text{Load}}^{\{hkl\}} - \sigma_{\text{Transverse}}^{\{hkl\}}$ (Equation (8)), these stresses have an impact on the calculated residual stresses. Here, the influence of the latter is expected to be more pronounced. At this point, the positive deviation indicates that the transverse stresses are in compression. The magnitude of the stress deviations due to the transverse stresses depends on the general mechanical properties (e.g., Young's modulus and Poisson's ratio). This explanation also applies to the LPBF IN718 sample. Knowing that the LPBF IN718 tensile samples were subjected to soft annealing heat treatment, the onset of plastic deformation is expected to start earlier due to the reduced yield strength. Furthermore, texture of the sample affects the mechanical properties.[21,45,63] However, further measurements need to be performed to explain these deviations comprehensively and exclude any other possible influencing factors, e.g., internal defects in the case of the LPBF tensile test sample. The anisotropy of microstructure in case of the LPBF IN718 has to be considered in addition to the potential explanations given earlier.

Obviously, the results obtained by Hooke's approach (Figure 10b and 11b) show a more pronounced deviation and noisiness in their pattern than those obtained by the proposed $\sin^2\alpha$ approach (Figure 10a and 11a). On the one hand, this could be somehow affected by the detector tilt in case this has not been entirely eliminated. On the other hand, the not fully occupied DSR (as is the case of the LPBF IN718) and, thus, the missing reflections in the necessary directions, i.e., $\alpha = 0°, 90°, 180°$, and $270°$, could be the reason for the miscalculation by Hooke's approach.

The $\sin^2\alpha$ approach and Hooke's approach should also be applicable similarly for the compression test; here, the measurements were not performed due to the geometry of the samples used.

Anyhow, for both cases the considered $\sin^2\alpha$ approach is characterized by superior stability and, thus, reliability. This is clearly proven by the residual stresses being directly induced by the loading stresses in the validation in situ tests detailed here.

3.4. Space-Resolved Residual Stress Measurements Using Sin²α Approach

In the following, as an application case, the residual stress mapping of the LPBF IN718 sample is evaluated using the $\sin^2\alpha$ approach. The LPBF IN718 sample was fabricated following the scanning strategy detailed before (cf. Section 2.1) and was characterized using synchrotron radiation in transmission mode. The analysis of area detector images covering the whole DSR patterns of many lattice planes is an essential aspect of the applied diffraction experiments. Based on such data, residual stresses can be determined robustly, and information related to peak intensities and profiles for a wide range of grain orientations can be analyzed. Furthermore, texture can basically be assessed by a single detector image; however, quantitative analysis is highly challenging.[64]

Due to masking/shadowing effects imposed by the sample holder during the measurement, some of the captured detector images were ill-defined and, thus, could not be evaluated (**Figure 12**a,b, 38 mm to the top).

In Figure 12a, the residual stress profile of the sample (for the lattice plane 311) is shown. The sample exhibits a characteristic profile: a tensile residual stress state at the sample edges prevails in addition to a compressive state in the sample interior. For instance, at 1 mm to the left and 17 mm to the top, the tensile residual stress is $\sigma_{\text{BD}-\text{TD}}^{311} = 755$ MPa, while a compressive residual stress $\sigma_{\text{BD}-\text{TD}}^{311} = -330$ MPa is seen at the same distance to the top, but 11 mm to the left.

In previous studies including data from simulation, it was observed that during the production of samples applying a bidirectional scanning strategy with 90° rotation, in each layer the middle region (layer cross-section) is the last position to cool due to the accumulation of residual heat.[65,66] This leads to a maximum deflection in the middle region. As a result, depending on the magnitude of the deflection, decreasing tensile residual stresses
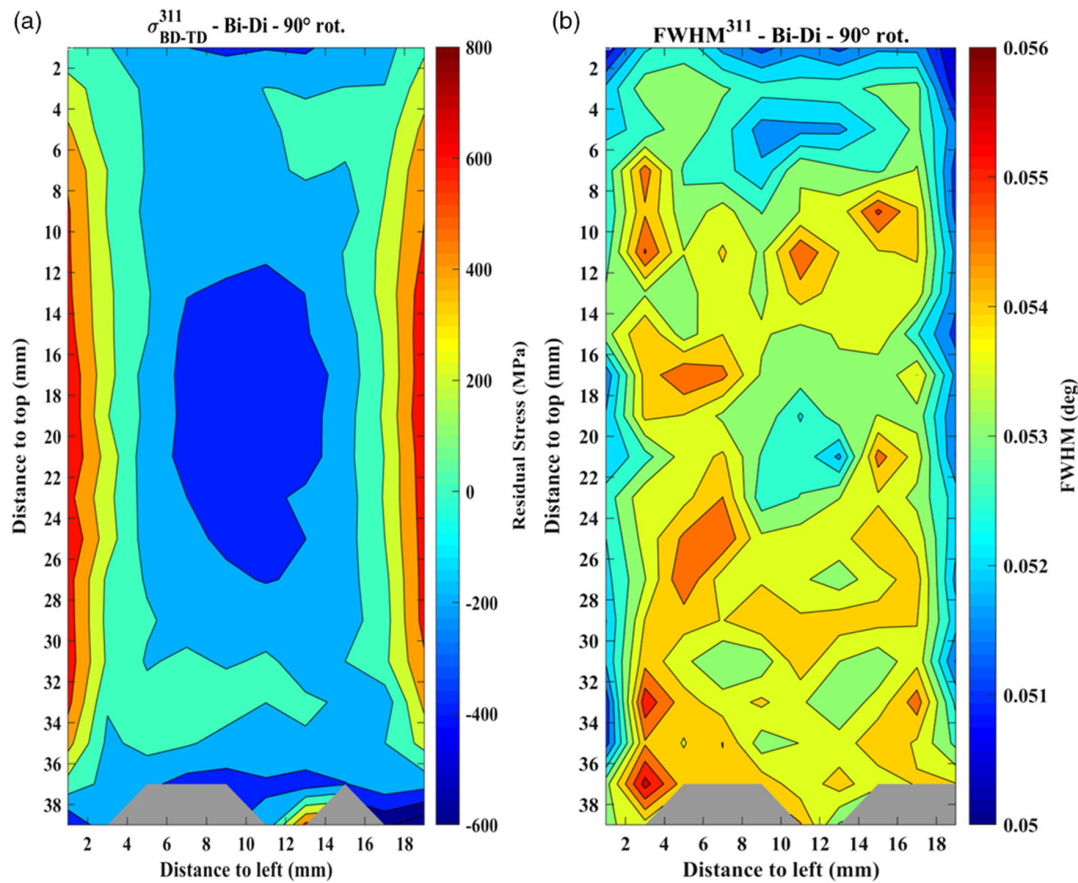
Figure 12. a) Residual stress and b) FWHM mapping of the 311 lattice plane of the LPBF IN718 sample processed according to the Bi-Di scan strategy being characterized by a 90° rotation between each layer.

from the center to the sample edges in TD can be observed. Corresponding to the fact that the measured stresses are a combination of the stresses in BD minus the stresses in TD it can be assumed that in the same region increasing compressive residual stresses in the direction of BD can occur. The results shown in Figure 12a are in good agreement with this assumption.

It is well known that the generation of residual stresses in AM samples is influenced not only by the scan strategy and, as a result, by the thermal history of the samples, but also by the sample geometry. Furthermore, residual stress relief has been reported as a consequence of sample detachment from the build platform. Furthermore, residual stress relief can occur in the lower layers while scanning the upper layers.[1] Furthermore, heat accumulation in the samples along the sample height during manufacturing should also be considered.[1,67] However, the investigation of these influences was not in the focus of present work.

The introduced $\sin^2\alpha$ approach is also sensitive to full width at half maximum (FWHM) values, which are evaluated in the form of mean values for each detected DSR, as shown for the 311 lattice plane in Figure 12b. The FWHM values decrease to the top and the edges of the sample. Caused by the complex, partly heterogeneous microstructure, the local variation of the FWHM values had to be expected. Regarding this perception, further analysis of the LPBF microstructure has to be conducted in further work.

4. Conclusion

In present work, a novel residual stress evaluation method based on linear regression, the $\sin^2\alpha$ approach, is proposed to be applied for synchrotron measurements in transmission mode to analyze locally different residual stresses in additively manufactured samples. The effect of local microstructural characteristics (such as texture, grain size, and morphology) on the experimentally determined strains seems to lead to miscalculations of the residual stresses using standardized approaches, such as Hooke's approach.

As a first step, simulated detector images with complete DSRs recorded using an area detector during synchrotron beam measurements in transmission mode were analyzed, and the residual stresses were calculated using both methods (Hooke's approach and $\sin^2\alpha$ approach). The simulations clearly revealed the robustness of the $\sin^2\alpha$ approach as compared to Hooke's approach.

In a second step, the $\sin^2\alpha$ approach was evaluated experimentally using in situ tensile tests on two tensile test samples of conventionally produced 100Cr6 steel and additively processed (LPBF) INCONEL 718. The same set of experimentally determined data were evaluated using both methods, where the $\sin^2\alpha$ approach shows better robustness in calculating residual stresses from both materials.

Finally, residual stress measurements were performed on a LPBF IN718 sample additively manufactured using a bidirectional scanning strategy with 90° rotation between each successive layer. Due to its unique characteristics, the $\sin^2\alpha$ approach seems to be very useful even for in situ measurements during AM processing, where the acquisition time for data is minimal. Thus, the method is excellent for taking advantage of fast measurements with high-intensity beams and multiple completely detectable DSRs on area detectors at synchrotron facilities.

Acknowledgements

Conflict of Interest

The authors declare no conflict of interest.

Data Availability Statement

Research data is not shared as this is part of an ongoing project.

Keywords

[1] P. Mercelis, J.-P. Kruth, *Rapid Prototyping J.* **2006**, *12*, 254.
[2] T. S. Srivatsan, T. S. Sudarshan, *Additive Manufacturing: Innovations, Advances, and Applications*, CRC Press, Boca Raton **2015**.
[3] M. Maniruzzaman, *3D and 4D Printing in Biomedical Applications: Process Engineering and Additive Manufacturing*, Wiley-VCH Verlag GmbH & Co. KGaA, Weinheim **2019**.
[4] F42 Committee, *Terminology for Additive Manufacturing – General Principles – Terminology*, ASTM International, West Conshohocken, PA.
[5] M. Strantza, R. K. Ganeriwala, B. Clausen, T. Q. Phan, L. E. Levine, D. C. Pagan, J. Ruff, W. E. King, N. S. Johnson, R. M. Martinez, V. Anghel, G. Rafailov, D. W. Brown, *Addit. Manuf.* **2021**, *45*, 102003.
[6] Z.-C. Fang, Z.-L. Wu, C.-G. Huang, C.-W. Wu, *Opt. Laser Technol.* **2020**, *129*, 106283.
[7] J. Robinson, I. Ashton, P. Fox, E. Jones, C. Sutcliffe, *Addit. Manuf.* **2018**, *23*, 13.
[8] X. Zhang, J. Kang, Y. Rong, P. Wu, T. Feng, *Materials (Basel, Switzerland)* **2018**, *12*.
[9] F. Azarmi, I. Sevostianov, *Curr. Opin. Chem. Eng.* **2020**, *28*, 21.
[10] W. Everhart, J. Dinardo, C. Barr, *Metall. Mater. Trans. A* **2017**, *48*, 697.
[11] H. Ali, H. Ghadbeigi, K. Mumtaz, *J. Mater. Eng. Perform.* **2018**, *27*, 4059.
[12] R. K. Ganeriwala, M. Strantza, W. E. King, B. Clausen, T. Q. Phan, L. E. Levine, D. W. Brown, N. E. Hodge, *Addit. Manuf.* **2019**, *27*, 489.
[13] H. Ali, L. Ma, H. Ghadbeigi, K. Mumtaz, *Mater. Sci. Eng.: A* **2017**, *695*, 211.
[14] P. Bian, J. Shi, Y. Liu, Y. Xie, *Opt. Laser Technol.* **2020**, *132*, 106477.
[15] L. Parry, I. A. Ashcroft, R. D. Wildman, *Addit. Manuf.* **2016**, *12*, 1.
[16] Y. Liu, Y. Yang, Di Wang, *Int. J. Adv. Manuf. Technol.* **2016**, *87*, 647.
[17] A. Ahmadi, R. Mirzaeifar, N. S. Moghaddam, A. S. Turabi, H. E. Karaca, M. Elahinia, *Mater. Des.* **2016**, *112*, 328.
[18] N. Nadammal, T. Mishurova, T. Fritsch, I. Serrano-Munoz, A. Kromm, C. Haberland, P. D. Portella, G. Bruno, *Addit. Manuf.* **2021**, *38*, 101792.
[19] H. Y. Wan, Z. J. Zhou, C. P. Li, G. F. Chen, G. P. Zhang, *J. Mater. Sci. Technol.* **2018**, *34*, 1799.
[20] E. Hosseini, V. A. Popovich, *Addit. Manuf.* **2019**, *30*, 100877.
[21] D. Deng, R. L. Peng, H. Brodin, J. Moverare, *Mater. Sci. Eng.: A* **2018**, *713*, 294.
[22] J. Günther, F. Brenne, M. Droste, M. Wendler, O. Volkova, H. Biermann, T. Niendorf, *Sci. Rep.* **2018**, *8*, 1298.
[23] M. E. Aydinöz, F. Brenne, M. Schaper, C. Schaak, W. Tillmann, J. Nellesen, T. Niendorf, *Mater. Sci. Eng.: A* **2016**, *669*, 246.
[24] F. Brenne, A. Taube, M. Pröbstle, S. Neumeier, D. Schwarze, M. Schaper, T. Niendorf, *Prog. Addit. Manuf.* **2016**, *1*, 141.
[25] T. Niendorf, S. Leuders, A. Riemer, H. A. Richard, T. Tröster, D. Schwarze, *Metall and Materi Trans B* **2013**, *44*, 794.
[26] H. L. Wei, J. Mazumder, T. DebRoy, *Sci. Rep.* **2015**, *5*, 16446.
[27] S. Schuster, J. Gibmeier, *Exp. Mech.* **2016**, *56*, 369.
[28] V. Hauk, H. Behnken, *Structural and Residual Stress Analysis by Nondestructive Methods: Evaluation – Application – Assessment*, Elsevier, Amsterdam **2006**.
[29] *Practical Residual Stress Measurement Methods* (Ed.: G. S. Schajer), Wiley, Chichester **2013**.
[30] R. Fernández, S. Ferreira-Barragáns, J. Ibáñez, G. González-Doncel, *Mater. Des.* **2018**, *137*, 117.
[31] *Measurement of Residual and Applied Stress Using Neutron Diffraction* (Eds.: M. T. Hutchings, A. D. Krawitz), Springer Science/Kluwer Academic, Dordrecht/Boston **1992**.
[32] C. Genzel, C. Stock, W. Reimers, *Mater. Sci. Eng.: A* **2004**, *372*, 28.
[33] B. Eigenmann, B. Scholtes, E. Macherauch, *Mat.-wiss. u. Werkstofftechnik* **1990**, *21*, 257.
[34] B. B. He, *Two-Dimensional X-Ray Diffraction*, Wiley, Hoboken, NJ **2009**.
[35] L. Spieß, G. Teichert, R. Schwarzer, H. Behnken, C. Genzel, *Moderne Röntgenbeugung*, Vieweg+Teubner, Wiesbaden **2009**.
[36] W. Chen, T. Voisin, Y. Zhang, J.-B. Florien, C. M. Spadaccini, D. L. McDowell, T. Zhu, Y. M. Wang, *Nat. Commun.* **2019**, *10*, 4338.
[37] T. Niendorf, F. Brenne, M. Schaper, A. Riemer, S. Leuders, W. Reimche, D. Schwarze, H. J. Maier, *Rapid Prototyping J.* **2016**, *22*, 630.
[38] L. Thijs, M. L. Montero Sistiaga, R. Wauthle, Q. Xie, J.-P. Kruth, J. van Humbeeck, *Acta Mater.* **2013**, *61*, 4657.
[39] F. Brenne, T. Niendorf, *Mater. Sci. Eng.: A* **2019**, *764*, 138186.
[40] A. Hollmann, M. Meixner, M. Klaus, C. Genzel, *J. Appl. Crystallogr.* **2021**, *54*, 22.
[41] K. Tanaka, *Mech. Eng. Rev.* **2019**, *6*, 1800378.
[42] K. Suzuki, *NDT E Int.* **2017**, *92*, 104.
[43] T. Mishurova, K. Artzt, J. Haubrich, S. Evsevleev, A. Evans, M. Meixner, I. S. Munoz, I. Sevostianov, G. Requena, G. Bruno, *Metall. Mater. Trans. A* **2020**, *51*, 3194.

[44] I. Serrano-Munoz, T. Fritsch, T. Mishurova, A. Trofimov, D. Apel, A. Ulbricht, A. Kromm, R. Hesse, A. Evans, G. Bruno, *J. Mater. Sci.* **2021**, *56*, 5845.

[45] J. Schröder, T. Mishurova, T. Fritsch, I. Serrano-Munoz, A. Evans, M. Sprengel, M. Klaus, C. Genzel, J. Schneider, G. Bruno, *Mater. Sci. Eng.: A* **2021**, *805*, 140555.

[46] Q. Jia, D. Gu, *J. Alloys Compd.* **2014**, *585*, 713.

[47] B. Zhang, Y. Li, Q. Bai, *Chin. J. Mech. Eng.* **2017**, *30*, 1476.

[48] A. Li, V. Ji, J. Lebrun, G. Ingelbert, *Exp Techniques* **1995**, *19*, 9.

[49] J. Maisenbacher, J. Gibmeier, K. Klimscha, T. Fischer, P. Staron, *Microsyst. Technol.* **2015**, *21*, 1787.

[50] M. Pröbstle, S. Neumeier, J. Hopfenmüller, L. P. Freund, T. Niendorf, D. Schwarze, M. Göken, *Mater. Sci. Eng.: A* **2016**, *674*, 299.

[51] ASM International, *ASM handbook*, ASM International, Materials Park, OH **1991**.

[52] I. C. Noyan, J. B. Cohen, *Residual Stress: Measurement by Diffraction and Interpretation*, Springer, New York **1987**.

[53] *Additive Manufacturing of Emerging Materials* (Ed.: B. AlMangour), Springer International Publishing, Cham **2019**.

[54] Z. Wang, E. Denlinger, P. Michaleris, A. D. Stoica, D. Ma, A. M. Beese, *Mater. Des.* **2017**, *113*, 169.

[55] P. J. Withers, M. Preuss, A. Steuwer, J. W. L. Pang, *J. Appl. Crystallogr.* **2007**, *40*, 891.

[56] A.-C. Dippel, H.-P. Liermann, J. T. Delitz, P. Walter, H. Schulte-Schrepping, O. H. Seeck, H. Franz, *J. Synchrotron Rad.* **2015**, *22*, 675.

[57] A. Ellermann, *Der Bauschingereffekt bei vergüteten, bainitischen und normalisierten Zuständen der Stähle 42CrMoS4 und 100Cr6*, Kassel University Press, Kassel **2013**.

[58] T. Manns, *Analyse oberflächennaher Eigenspannungszustände mittels komplementärer Beugungsverfahren*, Kassel University Press, Kassel **2011**.

[59] J. Kieffer, V. Valls, N. Blanc, C. Hennig, *J. Synchrotron Rad.* **2020**, *27*, 558.

[60] G. Ashiotis, A. Deschildre, Z. Nawaz, J. P. Wright, D. Karkoulis, F. E. Picca, J. Kieffer, *J. Appl. Crystallogr.* **2015**, *48*, 510.

[61] E. B. Knudsen, H. O. Sørensen, J. P. Wright, G. Goret, J. Kieffer, *J. Appl. Crystallogr.* **2013**, *46*, 537.

[62] N. Schell, A. King, F. Beckmann, T. Fischer, M. Müller, A. Schreyer, *MSF* **2013**, *772*, 57.

[63] M. Kamaya, *Int. J. Solids Struct.* **2009**, *46*, 2642.

[64] H.-R. Wenk, S. Grigull, *J. Appl. Crystallogr.* **2003**, *36*, 1040.

[65] B. Cheng, S. Shrestha, K. Chou, *Addit. Manuf.* **2016**, *12*, 240.

[66] T. Mukherjee, W. Zhang, T. DebRoy, *Comput. Mater. Sci.* **2017**, *126*, 360.

[67] R. Ranjan, C. Ayas, M. Langelaar, F. van Keulen, *Materials (Basel, Switzerland)* **2020**, *13*.

2100184 (15 of 15)